A Mathematical Model of Drying for Hygroscopic Porous Media

A mathematical model is developed to simulate the drying of hygroscopic porous media and, in particular, of wood. Drying rate experiments were performed using wood specimens and a nonhygroscopic porous ceramic solid and were simulated using the appropriate version of the drying model. Calculated model predictions are in very satisfactory agreement with experimental results. An examination of the relative impacts on drying of the transport mechanisms that comprise the model leads to meaningful interpretations of observed drying behavior. Controlling rate factors can be identified and different types of drying behavior specific to a given material or drying condition can be explained and understood through model simulation studies. Such capability can provide important guidance for drying process design and control.

M. A. Stanish, G. S. Schajer, Ferhan Kayıhan
Weyerhaeuser Technology Center
Tacoma, Washington 98477

SCOPE

The drying of moist porous solids is a complicated process involving simultaneous, coupled heat and mass transfer phenomena. Accordingly, drying behavior can be influenced by a rather large variety of independent factors, including, for example, ambient conditions of temperature, air velocity, and relative humidity, and solid properties such as density, permeability, and hygroscopicity. Extensive characterization of drying behavior using a strictly experimental approach constitutes a formidable challenge due to the excessively large number of variables that must be considered. The task becomes more manageable, however, with the help of a reliably realistic mathematical model of the drying phenomenon. Our objective is to develop such a tool to simulate drying behavior and therefore allow us to extend the results of experimental drying investigations. In this way, the impact of the many variables on drying behavior can be examined and interpreted without having to resort to an extensive program of experimental testing.

The approach taken here represents advancement of drying modeling and theory on several fronts. The mathematical description of the drying process is derived and maintained for the most general case; a comprehensive set of fundamental heat- and mass-transfer mechanisms is coupled with thermodynamic phase equilibrium expressions in a way that accommodates either hygroscopic or nonhygroscopic materials. Heat transfer by both conduction and convection is included together with mass transfer by gaseous diffusion and bulk flow of gas and liquid through the void space and by bound-water diffusion through the solid matrix. Bound-water migration is expressed in terms of the diffusion of sorbed water driven by the gradient in the chemical potential of the bound molecules. While this concept of bound-water diffusion was previously suggested by Siau (1983) and others (Kawai et al., 1978), in this development a new, uniquely explicit expression for bound-water flux is derived in terms of temperature and vapor pressure gradients. Combination of all of these transport mechanisms in a single generalized model has provided the first opportunity to examine their individual roles, collective interactions, and relative impacts on drying behavior.

Correspondence concerning this paper should be addressed to Ferhan Kayıhan.
M. A. Stanish is with Energy International, Inc., Bellevue, WA 98004.

SIGNIFICANCE AND CONCLUSIONS

A unique modeling approach based on fundamental heat and mass transfer relationships and thermodynamic equilibrium provides a tool that is effective in predicting drying behavior and also useful in exploring and understanding the impact of important variables on the drying process. The inherently more complicated computational problem resulting from this approach was handled efficiently by developing a reduced but mathematically equivalent set of governing equations and numerically solving them using a specialized solver and an adaptive mesh scheme. Comparisons of model predictions with experimental drying data helped to verify the model for both hygroscopic and nonhygroscopic drying.

Agreement between experimental results and model simulations was satisfactory; the model transport parameters used were consistent and reasonable based on current knowledge of wood physical properties. Model profiles of temperature and moisture concentrations were instrumental in interpreting observed drying rate behavior and identifying the rate-controlling processes.

With transport parameters derived from experimental drying tests using the material of interest, the model can be used to simulate drying for a variety of conditions or material properties. In this way, a data base for drying behavior can be generated. Alternatively, sensitivity studies can be performed to determine the effect of different material properties on specific drying behavior. In lumber processing, for example, given reasonable estimates for the range and distribution of wood properties represented within a lumber kiln charge, the corresponding distribution of expected drying behavior can be predicted. In summary, the model's simulation capabilities have significant implications in understanding drying behavior as well as in a range of application areas such as equipment design and process control.

Introduction

Although substantial efforts have already been devoted to the mathematical modeling of drying phenomena, the science remains far from perfected and therefore interest in the subject remains intense and widespread. Many of the previous approaches have been limited to very specific applications with regard to either the material being dried or the particular drying regime or mechanism at work. Extensive publications appear in the literature; however, a rigorous review is outside the scope of this paper. Compilations of recent developments appear in publications edited by Ashworth (1982) and Mujumdar (1980, 1983). Applications to lumber drying have been surveyed by Rosen (1983).

In the following sections, a full description is given of the conceptual model and underlying assumptions on which the mathematical equations of the model are based. The full set of equations is then presented, followed by a discussion of the methods employed for their numerical solution. Experimental drying test results using both hygroscopic and nonhygroscopic materials are then compared with model simulations in order to verify the model.

Model Development

The drying phenomenon is viewed as a process of simultaneous mass and energy transfer occurring both inside and outside the wood. Three moisture phases are recognized: free (liquid) water, bound water, and water vapor. Heat and mass transfer are coupled by the requirement that all phases remain in thermodynamic equilibrium at the local temperature. Thus evaporation rates are determined locally by the balance between heat flows, temperature changes, and moisture flows, all subject to phase equilibrium constraints. The overall drying phenomenon results from the simultaneous interaction of all of these processes.

The mechanisms of energy and mass transport are critical factors in such a conceptual description of drying. In this model, we try to identify all significant modes of transport and retain a quantitative mathematical expression for each. For example, an independent migration mechanism is postulated for each of the three moisture phases. Free water flows in bulk form driven by a gradient in the pressure within the liquid phase. Bound water migrates by a diffusion process that is driven by a gradient in the chemical potential of the sorbed water molecules. Water vapor and air are transported both by bulk flow driven by a gradient in total gas pressure and by binary diffusion driven by a gradient in the mole fraction of each component. Similarly, energy flows resulting from both conductive and convective mechanisms are included.

Modeling approach

1. Mass and energy transport are one-dimensional.
2. Gas, liquid, and solid are recognized as independent phases with characteristic properties. Moisture can exist in any of the three different phases: a vapor in the gas, as free liquid, or as bound water within the porous solid matrix.
3. Local thermal and phase equilibria are always obeyed. If free liquid is present, the vapor and bound phases remain saturated at the local temperature. In the absence of liquid, the bound water concentration and gas phase composition obey a sorption isotherm at the local temperature.
4. Conditions at the two boundaries are completely independent of each other, may vary with time, and are characterized by convective transfer coefficients.

5. Migration of the bound water through the solid matrix occurs by a molecular diffusion process having a flux proportional to the gradient in the chemical potential of the bound molecules.

6. Bulk convection of the liquid and gas phases follows Darcy's law. The effective permeability of the solid to both liquid and gas varies with the relative saturation of the void space within the solid.

7. Physical properties can vary with respect to both space and time. Transport properties that are dependent on changing physical properties therefore can also vary with respect to space and time.

Governing equations

The model equations contain five dependent variables, consisting of four mass densities and temperature. Densities are defined per unit volume of space in order to account for the porosity of the solid matrix. For drying, the four densities are identified as those of air, water vapor, bound water, and free water. The five dependent variables are described in terms of two independent variables, space and time. There are five governing equations: two mass balances (one each for air and for water), one energy balance, and two equilibrium equations (one describing vapor-liquid saturation and a second for the bound water sorption relation).

Material and Energy Balances. In order to include mass transfer contributions from bulk flow, a mass balance on air must be satisfied. The conservation equation for air is:

$$\frac{\partial}{\partial t}(\rho_a) = -\frac{\partial}{\partial z}(n_a) \tag{1}$$

The conservation equation for water is:

$$\frac{\partial}{\partial t}(\rho_v + \rho_b + \rho_f) = -\frac{\partial}{\partial z}(n_v + n_b + n_f) \tag{2}$$

By writing a balance equation for total water, we avoid having to specify explicitly the unknown rate of evaporation.

The energy balance is:

$$\frac{\partial}{\partial t}(\rho_a h_a + \rho_v h_v + \rho_b h_b + \rho_f h_f + \rho_d h_d) = -\frac{\partial}{\partial z}\left(n_a h_a + n_v h_v + n_b h_b^* + n_f h_f - k\frac{\partial T}{\partial z}\right) \tag{3}$$

The rate of evaporation need not appear explicitly since convective contributions from mass flow are included.

Phase Equilibrium Relations. If the local free water density is nonzero, the gas phase at that point is assumed saturated at the local temperature. Saturated water vapor densities from steam tables were correlated over the range 300–500 K to within 1% accuracy. The saturated water vapor density within the solid is given by:

$$\rho_v^{\text{sat}} = (\epsilon)\exp\left[-46.490 + 0.2179(T) - 5.0104\times10^{-4}(T)^2 + 3.4712\times10^{-7}(T)^3\right] \tag{4}$$

where the effective local void fraction is $\epsilon = \epsilon_d - (\rho_f/\rho_w)$ and the void fraction of dry solid is ϵ_d.

In the absence of free water, the gas phase is assumed to be saturated with respect to the local bound water content and temperature. Bound water sortpion data for wood were correlated by Simpson (1971). We use the inverted form of his equation to explicitly relate vapor density to the bound water content and the temperature:

$$\rho_v = \rho_v^{\text{sat}}\left\{a_4 + \left[(a_4)^2 + \frac{1}{a_1(a_2)^2}\right]^{1/2}\right\} \tag{5}$$

where:

$$a_1 = -45.70 + 0.3216(T) - 5.012\times10^{-4}(T)^2 \tag{6}$$

$$a_2 = -0.1722 + 4.732\times10^{-3}(T) - 5.553\times10^{-6}(T)^2 \tag{7}$$

$$a_3 = 1{,}417 - 9.430(T) + 1.853\times10^{-2}(T)^2 \tag{8}$$

$$a_4 = \frac{[1 - (18\rho_d/a_3\rho_b)]}{2a_2} - \frac{[1 + (18\rho_d/a_3\rho_b)]}{2a_1a_2} \tag{9}$$

Boundary conditions

Each of the three differential balance equations requires for solution an initial condition and two boundary conditions. To satisfy the first requirement, initial profiles must be specified for temperature and for air and water densities:

at $t = 0$:

$$T(z, 0) = T^o(z) \tag{10}$$

$$\rho_a(z, 0) = \rho_a^o(z) \tag{11}$$

$$\rho_v(z, 0) = \rho_v^o(z) \tag{12}$$

$$\rho_b(z, 0) = \rho_b^o(z) \tag{13}$$

$$\rho_f(z, 0) = \rho_f^o(z) \tag{14}$$

The initial moisture and temperature profiles must satisfy the local equilibrium constraints given by Eqs. 4 and 5.

The boundary condition requirements are satisfied by specifying three relations at each surface of the solid. First, the total gas pressure at each surface must equal the ambient pressure:

at $z = 0$:

$$p_a(0, t) + p_v(0, t) = p_{a_0}^{\infty}(t) + p_{v_0}^{\infty}(t) \tag{15}$$

at $z = L$:

$$p_a(L, t) + p_v(L, t) = p_{a_L}^{\infty}(t) + p_{v_L}^{\infty}(t) \tag{16}$$

where pressure is related to bulk density by $p = R\,T\,\rho/M\epsilon$.

Second, the total flux of moisture within the solid at each surface must equal the flux of water vapor through the external

boundary layer:

at $z = 0$:

$$n_v + n_b + n_f = \left\{x_v(N_v + N_a) + \mathscr{k}_{x_0}(t)\left[\frac{p^{\infty}_{v_0}(t)}{p^{\infty}_{a_0}(t) + p^{\infty}_{v_0}(t)} - x_v\right]\right\} M_v \quad (17)$$

at $z = L$:

$$n_v + n_b + n_f = \left\{x_v(N_v + N_a) + \mathscr{k}_{x_L}(t)\left[x_v - \frac{p^{\infty}_{v_L}(t)}{p^{\infty}_{a_L}(t) + p^{\infty}_{v_L}(t)}\right]\right\} M_v \quad (18)$$

In general, the convective mass transfer coefficients depend on the mass transfer rate itself; correlations derived from data for very low rates of mass transfer are corrected if mass fluxes become significant.

Third, the total energy flux within the solid at each surface must equal the total energy flux through the external boundary layer:

at $z = 0$:

$$n_a h_a + n_v h_v + n_b h^*_b + n_f h_f - k\frac{\partial T}{\partial z} = M_v N_v h_v + M_a N_a h_a + \mathscr{k}_0(t)[T^{\infty}_0(t) - T(0, t)] \quad (19)$$

at $z = L$:

$$n_a h_a + n_v h_v + n_b h^*_b + n_f h_f - k\frac{\partial T}{\partial z} = M_v N_v h_v + M_a N_a h_a + \mathscr{k}_L(t)[T(L, t) - T^{\infty}_L(t)] \quad (20)$$

Heat transfer coefficients are also dependent upon the rate of mass transfer and are corrected if necessary.

Transport phenomena

Mathematical relations for the flux terms in the governing material and energy balance equations are derived from fundamental equations for the appropriate transport mechanisms.

Liquid Phase. The migration rate of the free liquid phase is assumed to follow Darcy's law for flow through porous media. Therefore, the flux is proportional to the gradient in pressure within the liquid:

$$n_f = -\rho_w\left(\frac{K_f}{\eta_w}\right)\frac{\partial}{\partial z}(p_a + p_v - P_c) \quad (21)$$

where the total pressure within the liquid phase is equal to the total local gas pressure less the capillary pressure, P_c, associated with the gas-liquid interface. Spolek and Plumb (1981) measured capillary pressure in southern pine wood and suggested the following dependence on relative saturation (or fraction of void space occupied by liquid):

$$P_c = 10{,}000(\rho_f/\epsilon_d\rho_w)^{-0.61} \quad (22)$$

The relative permeability of the solid to liquid flow is dependent on the relative saturation and on the permeability of the solid when the voids are completely filled by liquid. Spolek and Plumb also reported that below a certain critical relative saturation, or irreducible saturation, the relative permeability fell to zero and liquid migration ceased due to a loss of continuity in the liquid phase. Above the irreducible saturation, the relative permeability increases with increasing relative saturation, often in a sigmoid manner (Tesoro et al., 1974). Thus, for wood the effective permeability is expressed by:

$$K_f = \begin{cases} 0; & \rho_f < \epsilon_d\rho_w s_{ir} \\ K^s_f\left\{1 - \cos\left[\dfrac{\pi}{2}\dfrac{(\rho_f/\epsilon_d\rho_w) - s_{ir}}{1 - s_{ir}}\right]\right\}; & \rho_f \geq \epsilon_d\rho_w s_{ir} \end{cases} \quad (23)$$

where s_{ir} is the irreducible saturation.

Gas Phase. The general expression of mass transport for the flux of component a in a binary gas mixture relative to stationary coordinates is:

$$n_a = \left[x_a(N_a + N_v) - c\,\mathscr{D}^{\text{eff}}\frac{dx_a}{dz}\right] M_a \quad (24)$$

With the convective or bulk-flow term expressed in the form of Darcy's law for flow through porous media, Eq. (24) gives the flux of air in terms of the dependent variables as:

$$n_a = -\left(\frac{\rho_a}{\epsilon}\right)\left(\frac{K_g}{\eta_g}\right)\frac{\partial}{\partial Z}(p_a + p_v) - \frac{M_a}{\epsilon}\left(\frac{\rho_a}{M_a} + \frac{\rho_v}{M_v}\right)\mathscr{D}^{\text{eff}}\frac{\partial}{\partial z}\left(\frac{p_a}{p_a + p_v}\right) \quad (25)$$

where the bulk flow rate depends on the relative permeability, K_g, and the molecular diffusion rate depends on the effective diffusivity, $\mathscr{D}^{\text{eff}}$. The flux of water vapor is given by a completely analogous equation with only the subscripts a and v interchanged.

In general, the effective diffusivity may be expressed as a random-pore gas diffusivity for porous solids:

$$\mathscr{D}_{rp} = \epsilon^2\,\mathscr{D}_{AB} \quad (26)$$

where ϵ accounts for both the volume occupied by the solid and the tortuosity of the void space. In wood, an additional attenuation factor α is used to account for closed pores resulting from the cellular nature of the solid. Since the bulk binary diffusivity of air-water vapor mixtures is given by:

$$\mathscr{D}_{AB} = 2.20 \times 10^{-5}\left(\frac{101{,}325}{p_a + p_v}\right)\left(\frac{T}{273.15}\right)^{1.75} \quad (27)$$

the effective diffusivity for wood drying is:

$$\mathscr{D}^{\text{eff}} = \alpha\,\mathscr{D}_{rp} = \frac{1.22 \times 10^{-4}\,(T)^{0.75}\,\epsilon^3\,\alpha}{R\,(\rho_a/M_a + \rho_v/Mv)} \quad (28)$$

The relative permeability of the solid to bulk gas flow is

dependent on the relative saturation and on the permeability of the solid when no liquid is present. For gas flow, the relative permeability decreases with increasing relative saturation. Although a sigmoidal dependence similar to the liquid relative permeability was suggested by Harmathy (1969), we assumed a simpler linear relationship given by:

$$K_g = K_g^d \frac{\epsilon}{\epsilon d} = K_g^d \left(1 - \frac{\rho_f}{\epsilon_d \rho_w}\right) \tag{29}$$

Bound Phase. The flux of bound water is assumed to be proportional to the gradient in the chemical potential of the bound molecules and to the volume fraction of space occupied by the cell wall matrix:

$$n_b = \mathcal{D}_b (1 - \epsilon_d) \frac{\partial \mu_b}{\partial z} \tag{30}$$

Since thermodynamic equilibrium is assumed at every location, the chemical potential of the bound molecules is by definition equal to the chemical potential of the vapor:

$$\mu_b \equiv \mu_v$$
$$d\mu_b \equiv d\mu_v \tag{31}$$

where, for gases:

$$M_v \, d\mu_v = -S_v \, dT + V \, dp_v \tag{32}$$

Therefore, the bound-water flux may be expressed in terms of the properties of the vapor phase by combining eqs. 30, 31, and 32 to form:

$$n_b = -\mathcal{D}_b (1 - \epsilon_d) \left[-\left(\frac{S_v}{M_v}\right) \frac{\partial T}{\partial z} + \left(\frac{\epsilon}{\rho_v}\right) \frac{\partial p_v}{\partial z} \right] \tag{33}$$

The entropy coefficient, S_v, may be evaluated using the thermodynamic relationship:

$$dS = \left(\frac{1}{T}\right) C_p \, dT - \left(\frac{R}{P}\right) dP \tag{34}$$

For water vapor as an ideal gas at 298.15 K and one atmosphere pressure, Moore (1972) lists the statistical and Third Law entropies as 185.3 and 188.7 $J/\text{mol} \cdot K$, respectively. Integration of Eq. (34) using an average value of 187 $J/\text{mol} \cdot K$ at 298.15 K and 101,325 Pa provides the following equation for S_v:

$$S_v = 187 + 35.1 \ln\left(\frac{T}{298.15}\right) - 8.314 \ln\left(\frac{p_v}{101{,}325}\right) \tag{35}$$

Siau and Babiak (1983) measured steady state nonisothermal moisture migration rates through white pine wood at moisture contents below fiber saturation. These data were analyzed using the flux expressions given by Eqs. 24 and 33 (Stanish, 1986). Table 1 contains a summary of the experimental conditions and results together with the corresponding theoretical migration rates predicted by the above equations. Diffusion parameters derived for this particular wood specimen are also listed. The close agreement between experiment and theory both supports the validity of the model equations and suggests appoximate values for the appropriate diffusion parameters.

Table 1. Experimental Conditions and Results

Data of Siau and Babiak (1983)

For all experiments	
Cool side temp.	= 35°C
Warm side temp.	= 70°C
Cool side dew point temp.	= 28.5°C
Cool side water vapor temp.	= 3.9 kPa

	Experiment No.			
	1	2	3	4
Warm side wet-bulb temp., °C	60	55	50	30
Warm side water vapor press., kPa	19	15	11	1.8
Avg. water flow, g/day	0.059	0.0	−0.048	−0.28
Total moisture flux × 10^8, kg/m² · s	−4.4	0.0	3.6	21

Optimal Diffusion Parameters and Calculated Fluxes for Data of Siau and Babiak

			Flux × 10^8, kg/m²/s			
	$\mathcal{D}_b$	$\alpha\epsilon^2$	Exp. 1	Exp. 2	Exp. 3	Exp. 4
Experimental	—	—	−4.4	0	3.6	21.0
Model Eqs.	1.8×10^{-14}	1.6×10^{-3}	−4.6	−0.2	4.4	20.8

Thermodynamic relationships

Enthalpy functions for each of the components are defined in terms of the model variables. For wood drying, the zero enthalpy reference state of each component was chosen to be 273.15 K and 101,325 Pa; heat capacities were assumed to be constant over the termperature range of interest. The enthalpies of air, free liquid water, and dry wood are then functions of temperature only:

$$h_a = 1{,}000(T - 273.15) \tag{36}$$

$$h_f = 4{,}180(T - 273.15) \tag{37}$$

$$h_d = 1{,}360(T - 273.15) \tag{38}$$

The enthalpy of water vapor is given by:

$$h_v = 4{,}180(T_{dp} - 273.15) + \lambda_{dp} + 1{,}950(T - T_{dp}) \tag{39}$$

Heat of vaporization data from steam tables were correlated with temperature using the polynomial:

$$\lambda = 2.792 \times 10^6 - 160(T) - 3.43(T)^2 \tag{40}$$

Combining Eqs. 39 and 40 gives the water vapor ethalpy as:

$$h_v = 1{,}950(T) + 1.65 \times 10^6 + 2{,}070(T_{dp}) - 3.43(T_{dp})^2 \tag{41}$$

Dew point temperature was correlated with partial water vapor

pressure by:

$$T_{dp} = 230.9 + 2.10 \times 10^{-4}(p_v) - 0.639(p_v)^{1/2} + 6.95(p_v)^{1/3} \quad (42)$$

The differential enthalpy of bound water at any concentration, or bound water content, is equal to the free water enthalpy less the differential heat of sorption. For wood, the differential heat of sorption is assumed to vary quadratically with bound water content and at zero bound water content to equal 40% of the heat of free water vaporization:

$$h_b^* = 4{,}180\,(T - 273.15) - 0.4\lambda\left(1 - \frac{\rho_b}{\rho_b^{fsp}}\right)^2 \quad (43)$$

where ρ_b^{fsp} is the bound water density at fiber saturation. The average bound water ethalpy for any given bound water content is obtained by integrating Eq. 43 and is given by:

$$h_b = 4{,}180\,(T - 273.15) - 0.4\lambda\left[1 - \frac{\rho_b}{\rho_b^{fsp}} + \frac{1}{3}\left(\frac{\rho_b}{\rho_b^{fsp}}\right)^2\right] \quad (44)$$

Physical properties

Data from steam tables for the density of liquid water were correlated with temperature using:

$$\rho_w = 1{,}157.8 - 0.5361(T) \quad (45)$$

The viscosity of an air-water vapor mixture is obtained from a linear combination of the component viscosities, weighted by the mole fractions in the mixture:

$$\eta_g = \{[4.06 \times 10^{-8}(T) + 6.36 \times 10^{-6}]\,P_a + [3.80 \times 10^{-8}(T) - 1.57 \times 10^{-6}]\,p_v\}/(p_a + p_v) \quad (46)$$

The viscosity of liquid water is given by Weast (1974) as the following function of temperature:

$$^{\log}10\,(\eta_w) = -13.73 + \frac{1{,}828}{(T)} + 1.966 \times 10^{-2}(T) - 1.466 \times 10^{-5}(T)^2 \quad (47)$$

The thermal conductivity of wood is adequately described for all moisture contents by:

$$k = (\rho_d/1{,}000)\left[0.40 + 0.50\left(\frac{\rho_v + \rho_b + \rho_f}{\rho_d}\right)\right] + 0.024 \quad (48)$$

Numerical Procedure

The five governing equations, Eqs. 1–5, were solved using a finite-space/continuous-time approach. We approximated the spatial derivatives in finite-difference form following the procedure described by Patankar (1980) and then numerically integrated the resulting ordinary differential equations using a specialized solver for stiff equations. This approach combines the conceptual simplicity of a finite-difference formulation with the numerical power of a robust solver to handle the stiffness of the equations. Since convective heat flows could be comparable to or larger than conductive flows, we used the hybrid upwinding scheme described by Spalding (1972) to keep the discretization stable.

For this one-dimensional model, the finite-difference mesh is just a single line of points. For each mesh point, the five dependent variables describe the local state of the material. All other quantities, for example, total pressure, can be derived from the five variables. After differentiation, Eqs. 1–5 for a single mesh point become:

$$\begin{vmatrix} 1 & 0 & 0 & 0 & 0 \\ 0 & 1 & 1 & 1 & 0 \\ h_a & h_v & h_b^* & h_f & C \\ 0 & 0 & 0 & 0 & 0 \\ 0 & 0 & 0 & 0 & 0 \end{vmatrix} \frac{d}{dt} \begin{vmatrix} \rho_a \\ \rho_v \\ \rho_b \\ \rho_f \\ T \end{vmatrix} = \begin{vmatrix} \mathcal{A} \\ \mathcal{M} \\ \mathcal{E} \\ \mathcal{V} \\ \mathcal{B} \end{vmatrix} \quad (49)$$

where $\mathcal{A}$, $\mathcal{M}$, and $\mathcal{E}$ are finite-difference approximations to the flux terms on the righthand sides of Eqs 1, 2, and 3. The fourth and fifth rows represent the equilibrium conditions, Eqs. 4 and 5. The quantities $\mathcal{V}$ and $\mathcal{B}$ are the residuals computed by substituting the actual dependent variable values in the homogeneous forms of the equilibrium expressions. When equilibrium is satisfied, the fourth and fifth rows both reduce to the trivial equation, $0 = 0$.

Equation 49 can very easily be adapted to handle a nonhygroscopic porous material. In this case, there is no bound water, so there is one less dependent variable and one less equilibrium condition. Eq. 49 could be solved directly using a solver that accepts a set of coupled differential-algebraic equations (Hindmarsh, 1980). We developed a more computationally efficient approach by reducing the number of variables per mesh point from five to three. A new total moisture density variable $\rho_m = \rho_v + \rho_b + \rho_f$ replaces the three separate moisture variables. Also, the two equilibrium equations, Eqs. 4 and 5, are incorporated into the three balance equations, Eqs. 1, 2, and 3, rather than expressed explicitly as in Eq. 49. With these changes, Eq. 49 becomes

$$\frac{d}{dt}\begin{vmatrix} \rho_a \\ \rho_m \\ T \end{vmatrix} = \begin{vmatrix} \mathcal{A} \\ \mathcal{M} \\ \mathcal{C} \end{vmatrix} \quad (50)$$

where the value of $\mathcal{C}$ is computed by substituting the first two rows of Eq. 49 and the equilibrium expressions, Eqs. 4 and 5 into the third row of Eq. 49. Since Eq. 50 is in explicit form, we could use a less specialized ordinary differential equation solver. The LSODES program developed by Hindmarsh (1983) effectively handles the stiff system of equations encountered here. Additionally, this particular solver uses a knowledge of the sparsity structure of the Jacobian matrix to avoid redundant computation of zero-valued Jacobian entries.

At the start of each righthand-side evaluation for Eq. 50, the formulation separates the individual moisture phases from the

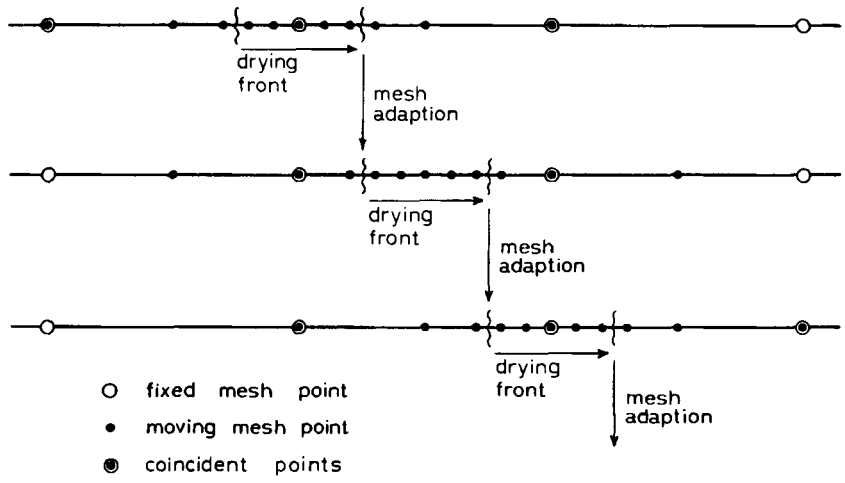

Figure 1. Diagram of the adaptive mesh scheme.

total moisture using the vapor and bound water equilibrium relationships. It then uses all five dependent variables to compute the heat and mass flow quantities $\mathcal{A}$, $\mathcal{M}$, and $\mathcal{E}$. Finally, the formulation uses the equilibrium relations again to calculate the quantity $\mathcal{C}$. In this way, the differential equation solver only handles the three dependent variables ρ_a, ρ_m, and T, while the rest of the formulation uses all five dependent variables.

The formulation uses the same numerical procedure throughout the modeled domain. To maintain discretization accuracy, we developed the adaptive finite-difference mesh scheme shown in Figure 1 to concentrate the mesh points and numerical effort around regions with rapidly changing properties, e.g., a wet-line drying front. The open circles represent a fixed coarse mesh, and the filled circles a superimposed fine mesh. As the front advances, the fine mesh points move forward so as to always enclose the front. During a mesh adaption, the air and moisture densities are redistributed by associating air and moisture masses with each old mesh point and apportioning those masses to the new mesh points. This scheme ensures that there is no overall change in mass during a mesh adaption. The same algorithm, when applied to the temperature values, gives a temperature interpolation weighted by the mesh point spacings. Since the finite-difference mesh is uniform around the drying front, the adaptive mesh scheme gives results essentially identical to those from a uniform nonadaptive mesh with the same fine-mesh point spacing. However, the adaptive mesh scheme requires two to five times less computation time than the equivalent nonadaptive mesh.

Experimental

Testing of the model's computational performance and verification of its predictions were performed for both hygroscopic and nonhygroscopic drying. Wood drying specimens consisted of 40 cm long sections of green 2 × 6 in. (5 × 15 cm) southern pine and Douglas fir lumber. The four side surfaces were coated with Chek-Ban moisture sealer in order that the drying would take place through only the upper and lower faces and therefore that moisture transport would remain one-dimensional. Drying of several pairs of end-matched specimens (each pair cut from the same board), one sample from each pair treated in this way and the other sealed on four sides with a coating of silicone sealant and a layer of 3 mm thick rubber sheet, all held to the specimen by screwed-on aluminum plates, confirmed the effectiveness of the simpler treatment. In the interest of simplicity and time savings, the former was therefore used in all testing. Thermocouples were glued into pre-drilled holes with silicone sealant at three depths: at the centerline, midway between the upper surface and the centerline (quarterline), and within approximately 1 mm of the surface. These thermocouples entered from the long side and extended approximately 8 cm into the wood.

Drying rate experiments were also performed using a porous ceramic brick measuring 22.7 × 10.4 × 3.2 cm and weighing 1.55 kg dry. After repeated pressure-vacuum impregnation cycles, the brick absorbed a maximum of approximately 200 g of water. The saturated brick was inserted flush into a well that had been machined in a 40 cm long section of dry 2 × 6 in. lumber, as shown schematically in Figure 2. The side and bottom surfaces of the brick were sealed with 3 mm thick rubber sheets, ensuring a tight fit, preventing moisture loss from those five sur-

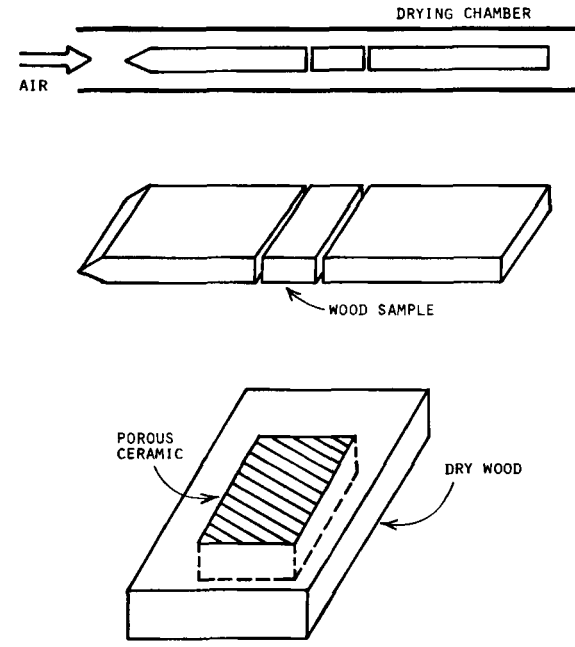

Figure 2. Diagram for drying experiments.

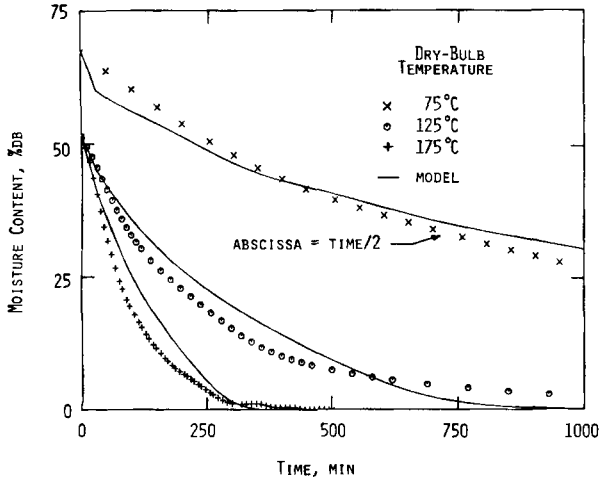

Figure 3. Comparison of model simulation results with experimental data for drying of end-matched southern pine lumber specimens at different temperatures.

Air velocity, 13 m/s; dew point, 10°C.

faces, and providing thermal insulation between the brick and wood. A thermocouple inserted to the center of the brick measured internal temperature.

Drying rate experiments were performed in a specially designed drying chamber, depicted in Figure 2. The specimen was suspended from a load cell and positioned so that its upper and lower surfaces were flush with an air flow divider both upstream and downstream of the sample. Air at controlled, measured dry bulb temperature, dew point temperature, and linear velocity was circulated past the specimen, and sample weight and internal temperatures were recorded with time. Flow in the channel below the specimen was blocked in the porous brick tests.

Results and Discussion

The results of experimental drying tests using wood specimens and a porous ceramic solid were compared with model

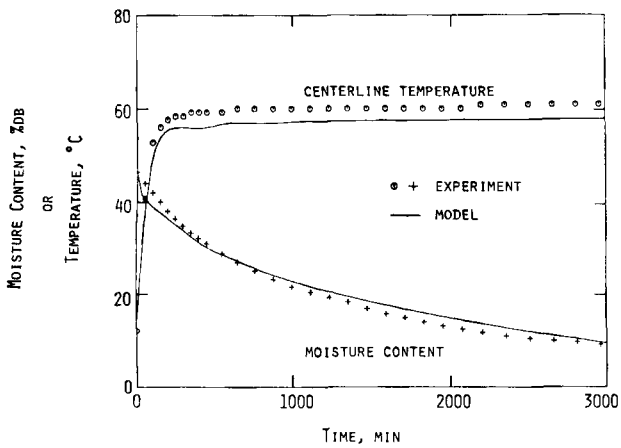

Figure 4. Comparison of model simulation results with experimental data for drying of southern pine lumber.

Temperature, 75°C; air velocity, 7 m/s; dew point, 10°C.

simulations both to verify the model predictions and to derive appropriate transport parameter values. The results of these activities are summarized here. Model simulation results are compared with experimental drying data in Figure 3 through 9. For those model parameters that could not be estimated by independent means, appropriate values were obtained by fitting the simulation results to a base set of experimental drying data. The data for end-matched samples of southern pine dried at 75, 125, and 175°C were chosen as the base set for all experiments with the same species; fitting the simulation results to these data yielded the following set of model parameters:

$$K_g^d = 5.0 \times 10^{-15}\, m^2$$

$$K_f^s = 5.0 \times 10^{-16}\, m^2$$

$$\alpha = 0.05$$

$$\mathcal{D}_b = 3.0 \times 10^{-13}\, kg/m^3/s$$

$$s_{ir} = 0.1$$

$$\mathcal{k} = 87\ W/m^2/K$$

Figure 3 shows a comparison of the model fit with the experimental data; close agreement was obtained at all three drying temperatures.

One aspect of model verification was to compare drying data from experiments run under different conditions with model simulations using the parameter values obtained from the base data. Results from a different pine specimen (cut from a different board) dried at 75°C, together with internal temperature data, are shown in Figure 4. All model parameters were the same as those listed above except the external heat and mass transfer coefficients, which were lower owing to the reduced air velocity; transfer coefficients varied with air velocity to the 0.6 power, as for fully-developed turbulent flow between parallel plates (Rohsenow and Hartnett, 1973), e.g., $\mathcal{k} = 58$ W/m^2/K at 7 m/s. These model simulations indicate that at 75°C, the external wood surface dries very rapidly with an accompanying rise of the internal temperature. A wet-line drying front appears, with the wood outside below the fiber saturation point and that inside still retaining some liquid water. The liquid water is conveyed from the interior to the drying front, but at a rate slower than the transport of moisture from the front to the wood surface. The front therefore travels inward through the wood as drying proceeds.

Simulation data also show that throughout the drying, the temperature drop across the external gas boundary layer is much larger than the temperature difference between the external surface and the interior of the wood. At the same time, the drop in water vapor concentration across the boundary layer is very small compared to that between the external surface and the wet-line drying front. These observations suggest that at this drying temperature, both external heat transfer and internal moisture transport play important roles in determining the drying rate.

The effects of drying air dew point and of drying air velocity on drying behavior were investigated in experiments at 125°C with end-matched specimens of southern pine. As shown in Figure 5, both the experimental and simulation results from the dew point study indicate that dew point has little impact on drying rate at 125°C over the range of dew points examined. The model again indicates that the wood surface dries rapidly, gen-

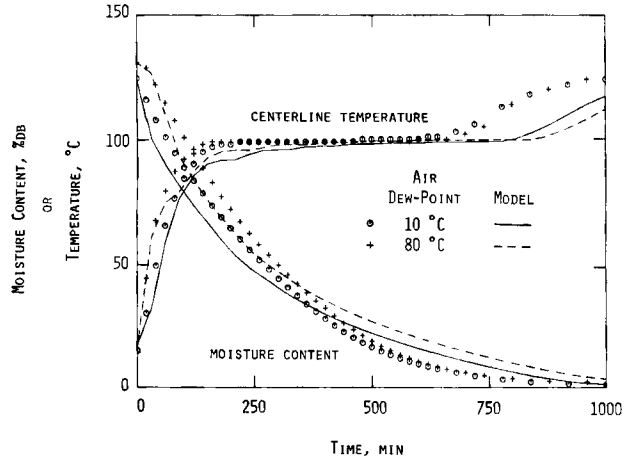

Figure 5. Comparison of model simulation results with experimental data for drying of end-matched southern pine lumber specimens at different dew points.

Temperature, 125°C; air velocity, 7 m/s.

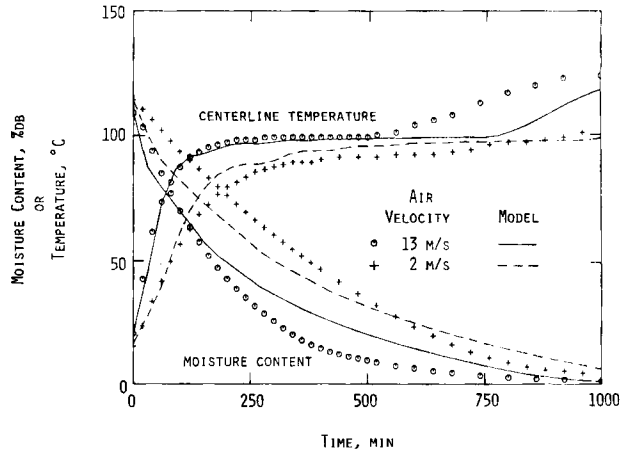

Figure 6. Comparison of model simulation results with experimental data for drying of end-matched southern pine lumber specimens at different air velocities.

Temperature, 125 °C; dew point, 10°C.

erating a wet-line drying front. Internal temperature rises to approximately 100°C and the pressure of the gas phase, which at the drying front consists entirely of water vapor, remains very close to one atmosphere. These simulation results suggest that the liquid water boils in the pores at the drying front. The water vapor produced is conveyed primarily by bulk flow to the external surface. After the front reaches the center of the wood and the last liquid water vanishes, the centerline temperature rises above 100°C.

Model results also show that initially, the temperature drop across the external boundary layer again is much larger than the temperature difference between the wood surface and interior. However, as the drying front recedes, the temperature drop between the wood surface and the drying front grows while that across the external boundary layer shrinks. Near the end of the drying period, the temperature difference across the wood layer dominates. Since the gas permeability of the wood is high enough that it apparently offers little resistance to gas flow at these fluxes, moisture transport is not rate-limiting. Drying at this temperature is mainly heat transfer-controlled. Furthermore, this control shifts from external to internal as drying progresses. Additional support for this mechanistic interpretation is provided by the observation that at this temperature dew point has virtually no effect on pine drying rates. This result is expected if drying is controlled by external and internal heat transfer rates, which are not affected by water vapor concentration to any appreciable extent.

Experimental and simulation results for pine drying at 125°C and different air velocities are shown in Figure 6. Model parameters were again identical to those above, with heat transfer coefficients $\mathscr{k} = 87\ \mathrm{W/m^2/K}$ and $\mathscr{k} = 29\ \mathrm{W/m^2/K}$ for the tests at 13 and 2 m/s, respectively. Agreement between experimental data and simulation results is very satisfactory. At this drying temperature, air velocity has a significant effect on drying rate, as is expected if the drying behavior is partially controlled by external heat transfer phenomena as explained above.

Drying test and model simulation results for drying of Douglas fir at 125°C are shown in Figure 7. A new set of model parameters was established for this wood species, with values as follows:

$$K_g^d = 1.0 \times 10^{-15}\ m^2$$
$$K_f^s = 5.0 \times 10^{-16}\ m^2$$
$$\alpha = 0.01$$
$$\mathcal{D}_b = 3.0 \times 10^{-13}\ kg/m^2/s$$
$$s_{ir} = 0.1$$
$$\mathscr{k} = 87\ W/m^2/K$$

Compared to results from the pine experiments, the internal temperatures in these experiments rise above 100°C earlier in the drying process. With both the gas permeability and the binary attenuation factor smaller than those for pine, the internal water vapor pressure at the drying front must rise slightly above 1 atm to provide sufficient pressure driving force for bulk

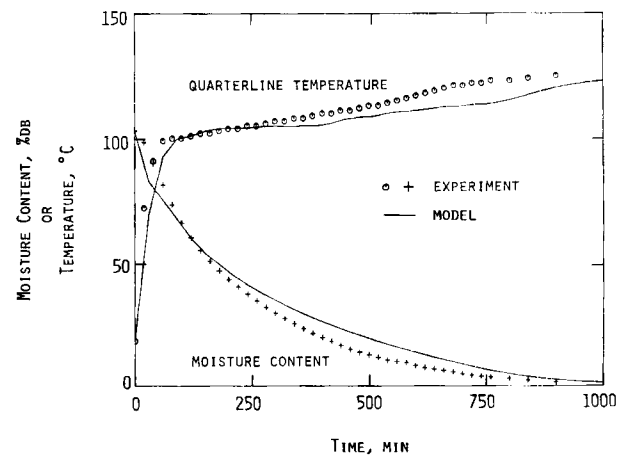

Figure 7. Comparison of model simulation results with experimental data for drying of Douglas fir lumber.

Temperature, 125°C; air velocity, 13 m/s; dew point, 10°C.

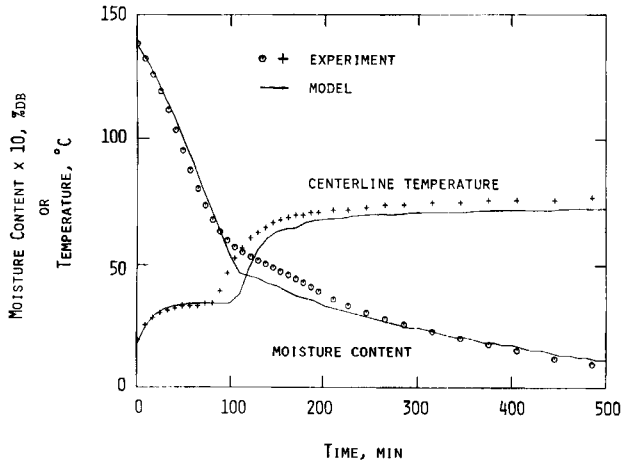

Figure 8. Comparison of model simulation results with experimental data for brick drying.
Temperature, 75°C; air velocity, 7 m/s; dew point, 10°C.

water vapor transport to the exterior. Since the water vapor pressure is above 1 atm, the temperature of the liquid may exceed 100°C.

Model stimulation results are compared with experimental data for porous ceramic brick drying at 75 and 125°C in Figure 8 and 9, respectively. Simulation parameters for the nonhygroscopic version of the model were identical in each case, as follows:

$$K_g^d = K_f^s = 5 \times 10^{-14}\ \text{m}^2$$

$$\alpha = 1$$

$$s_{ir} = 0.32$$

$$\mathscr{k} = 58\ \text{J/m}^2\text{/s/K}$$

Simulation results and experimental data are in close agreement at both drying temperatures. The brick drying behavior exhibits two sharply distinct stages. Initially, the drying rate is very high and the brick temperature remains low. In this first regime, liquid water migrates to the surface nearly as rapidly as

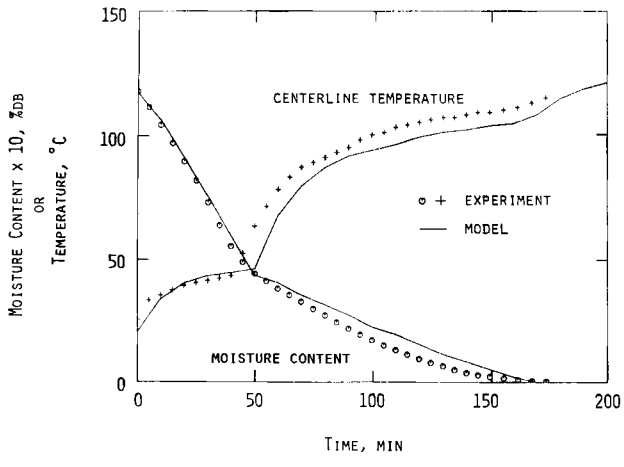

Figure 9. Comparison of model simulation results with experimental data for brick drying.
Temperature 125°C; air velocity, 7 m/s; dew point, 10°C.

it evaporates from the surface, and thus the drying rate is determined by the rates of external heat and mass transfer. The material behaves essentially as a wet bulb. However, when the surface moisture content reaches irreducible saturation, liquid can no longer be replenished at the surface. Shortly thereafter, the surface becomes dry and a drying front begins moving inward through the brick. At this time, the brick temperature begins rising and the drying rate falls substantially. In this second regime, drying behavior is analogous to that of the wood specimens at the same drying temperature. At 75°C the drying rate is controlled primarily by external heat transfer and internal water vapor diffusion, while at 125°C, the rate is controlled primarily by external and internal heat transfer.

The results described above demonstrate that the drying model closely simulates both hygroscopic and nonhygroscopic drying behavior using consistent sets of fundamental physical and transport parameters. While this in itself is a useful result, the significance of this simulation approach and the resulting model goes beyond the prediction of drying rate curves using generalized parameter sets for different families of materials.

Verifying the model with experimental drying data obtained from different wood samples revealed that with relatively minor changes in the model parameter set, agreement between experimental data and simulation results was improved beyond that shown in Figure 3 through 7. The magnitude of variation in the individual physical and transport parameters was well within ranges generally attributed to biological variation among different wood specimens of the same species. We therefore conclude that this model can simulate real differences in drying behavior that are due to physical variability among individual specimens of materials such as wood. This represents a level of simulation performance to our knowledge not previously attained in the drying field, and which we attribute to the use of fundamental thermodynamic and heat and mass transfer expressions and to rigorous solution of the resulting equation set.

Notation

a_1, a_2, a_3, a_4 = parametric functions for bound water sorption correlation, Eqs. 6, 7, 8, and 9
C = specific heat of wet wood, J/kg/K
C_P = heat capacity, J/mol/K
c = molar density mol/m^3
$\mathcal{D}^{\text{eff}}$ = effective gas diffusivity, m^2/s
$\mathcal{D}_{AB}$ = bulk binary diffusivity for air-water vapor mixtures, m^2/s
$\mathcal{D}_b$ = bound water diffusivity, kg/s/m^3
$\mathcal{D}_{rp}$ = effective random-pore gas diffusivity, m^2/s
H = enthalpy, J/mol
h = enthalpy, J/kg
h^* = differential enthalpy, J/kg
$\mathscr{k}$ = external heat transfer coefficient at the solid surface, J/m^2/s/K
K = effective permeability of moist solid, m^2
K_d = permeability of dry solid, m^2
K_s = permeability of saturated solid, m^2
k = thermal conductivity of moist solid, J/m/s/K
$\mathscr{k}_x$ = external mass transfer coefficient at the solid surface, mol/m^2/s
L = solid thickness, m
M = molecular weight, kg/mol
N = molar flux at the solid surface, mol/m^2/s
n = flux, kg/m^2/s
P = pressure, Pa
P_c = capillary pressure, Pa
p = partial pressure, Pa
p^∞ = ambient partial pressure at end of solid, Pa

R = gas constant, J/mol/K
S = entropy, J/mol/K
s_{ir} = irreducible saturation
T = temperature, K
T^o = initial temperature profile within the solid, K
T^∞ = ambient temperature at end of solid, K
t = time, s
V = molar volume, m^3/mol
x_v = mole fraction of water vapor in the gas at the solid surface
z = spatial variable, m

Greek letters

α = attenuation factor for vapor diffusivity in wood
ϵ = void fraction
η = viscosity, kg/m · s
λ = heat of vaporization, J/kg
μ = chemical potential, J/kg
ρ = density, kg/m^3
ρ^o = initial density within the solid, kg/m^3

Subscripts

a = air
b = bound water
d = dry wood
dp = dew point
f = free water
g = gas
v = water vapor
w = liquid water

Literature Cited

Ashworth, J. C., *Proc. 3rd Int. Drying Symp.*, Drying Research Limited, Wolverhampton, England, **1 & 2** (1982).

Harmathy, T. Z., "Simultaneous Moisture and Heat Transfer in Porous Systems with Particular Reference to Drying," *Ind. Eng. Chem. Fund.*, **8**(1), 92 (1969).

Hindmarsh, A. C., "LSODE and LSODE I, Two New Initial Value Ordinary Differential Equation Solvers," *ACM-SIGNUM Newsletter*, **15**(4), 10 (1980).

Hindmarsh, A. C., "ODEPACK, A Systematized Collection of ODE Solvers," *Proc. 10th IMACS World Con. Systems, Simulation and Sci. Comput.*, Montreal (1983).

Kawai, S., Nakato, K., and Sadoh, T., "Moisture Movement in Wood Below the Fiber Saturation Point," *Mokuzai Gakkaishi*, **24**(5), 273 (1978).

Moore, Walter J., *Physical Chemistry*, 4th ed., Prentice-Hall, Englewood Cliffs, New Jersey, 191 (1972).

Mujumdar, A. S., *Advances in Drying*, Hemisphere Pub., Washington, D.C. **1** (1980), **2** (1983).

———*Drying '80*, **1** & **2** (1980), *Drying '82* (1982), Hemisphere Pub., Washington, D.C.

Patankar, S. V., *Numerical Heat Transfer and Fluid Flow*, McGraw-Hill, New York (1980).

Rosen, H. N., "Recent Advances in the Theory of Drying Lumber," North Central Forest Experiment Station, Forest Service, U.S. Department of Agriculture (1983).

Rohsenow, W. H., and J. P. Hartnett, eds., *Handbook of Heat Transfer*, McGraw-Hill, New York (1973).

Siau, J. F., "Chemical Potential as a Driving Force for Nonisothermal Moisture Movement in Wood," *Wood Sci. Technol.*, **17**, 101 (1983).

Siau, J. F., and M. Babiak, "Experiments on Nonisothermal Moisture Movement in Wood," *Wood Fib. Sci.*, **15**(1), 40 (1983).

Simpson, W. T., "Equilibrium Moisture Content Prediction for Wood," *For. Prod. J.*, **21**(5), 48 (1971).

Spalding, D. B., "A Novel Finite-Difference Formulation for Differential Expressions Involving both First and Second Derivatives," *Int. J. Numerical Methods in Eng.*, **4**(4), 551 (1972).

Spolek, G. A., and Plumb, O. A., "Capillary Pressure in Softwoods," *Wood Sci. Technol.*, **15**, 189 (1981).

Stanish, M. A., "The Roles of Bound Water Chemical Potential and Gas Phase Diffusion in Moisture Transport through Wood," *Wood Sci. Technol.* (1986).

Tesoro et al., "Relative Permeability and the Gross Pore Structure of Wood," *Wood Fiber*, **6**(3), 226 (1974).

Weast, R. C., ed., *Handbook of Chemistry and Physics*, 56th ed., CRC Press, Cleveland, p. F49 (1974).

Wood Handbook, U.S. Forest Products Laboratory, Forest Service, U.S. Department of Agriculture (1955).

Manuscript received Feb. 28, 1985, and revision received Dec. 26, 1985.